Stress-driven tissue fluidization physically segments vertebrate somites

Elijah R. Shelton[1,*], Sangwoo Kim[1], Ben J. Gross[1], Ray Wu[2], Marie Pochitaloff[1], Irene Lim[3], Ellen M. Sletten[3] and Otger Campàs[1,2,4,5,6,*]

[1]*Department of Mechanical Engineering, University of California, Santa Barbara, CA 93106, USA*

[2]*Department of Molecular, Cellular and Developmental Biology, University of California, Santa Barbara, CA 93106, USA*

[3]*Department of Chemistry and Biochemistry, University of California, Los Angeles, CA 90095, USA*

[4]*Center for Bioengineering, University of California, Santa Barbara, CA 93106, USA*

[5]*California NanoSystems Institute, University of California, Santa Barbara, CA 93106, USA*

[6]*Cluster of Excellence Physics of Life, TU Dresden, 01062 Dresden, Germany*

*Correspondence should be addressed to Elijah R. Shelton (eshelton@ucsb.edu) or Otger Campàs (campas@ucsb.edu)

Shaping functional structures during embryonic development requires both genetic and physical control. During somitogenesis, cell-cell coordination sets up genetic traveling waves in the presomitic mesoderm (PSM) that orchestrate somite formation. While key molecular and genetic aspects of this process are known, the mechanical events required to physically segment somites from the PSM remain unclear. Combining direct mechanical measurements during somite formation, live imaging of cell and tissue structure, and computer simulations, here we show that somites are mechanically sectioned off from the PSM by a large, actomyosin-driven increase in anisotropic stress at the nascent somite-somite boundary. Our results show that this localized increase in stress drives the regional fluidization of the tissue adjacent to the forming somite border, enabling local tissue remodeling and the shaping of the somite. Moreover, we find that active tension fluctuations in the tissue are optimized to mechanically define sharp somite boundaries while minimizing somite morphological defects. Altogether, these results indicate that mechanical changes at the somite-somite border and optimal tension fluctuations in the tissue are essential physical aspects of somite formation.

During embryonic development, signaling events coordinate cell behaviors to form functional structures, including organs and embryonic precursors of adult structures [1,2]. The molecular players and mechanisms involved in orchestrating morphogenesis, both in early embryos and during organ formation, have been studied extensively [1]. However, sculpting embryonic structures also involves spatiotemporal variations in tissue mechanics that progressively bring the tissue into shape [3–5]. In this sense, embryonic tissues are active materials with the remarkable ability to self-shape, but it remains unclear how this is achieved in specific cases.

The segmentation of the vertebrate body along its anteroposterior (AP) axis into periodic, bilaterally symmetric pairs of somites, or somitogenesis (Supplementary Movie 1), is a key process in vertebrate development that lays the foundation for all skeletal muscles and vertebrae in adults [6–9]. Several signaling pathways are involved in coordinating cell behaviors in space and time during the segmentation process [6,10,11]. Synchronization of genetic oscillators in neighboring cells of the PSM sustain traveling waves in the tissue that emerge at the posterior end of the body [8,12–14], travel anteriorly and eventually arrest, defining the location of the new somite along the AP axis [8,10,13,15]. Eph-ephrin interactions between cells at the prospective somite boundary regulate Rho and Rac activity [16–19], boundary cell de-adhesion and ECM deposition [20–22], defining the initial molecular signatures of mechanical changes during somitogenesis. However, the tissue-scale mechanical transformations that emerge from all these molecular events and shape the somites are unknown.

Mechanics has long been recognized to play a role in somite morphogenesis [23–26]. Previous observations of rounding and spontaneous segmentation of mesodermal explants in chick and quail [27], as well as the rounding of explanted somite tissue in zebrafish [28], suggested that tissue surface tension alone may drive segmentation, akin to a Plateau-Rayleigh instability in fluids [29]. However, recent experiments have shown that the PSM tissue is in a solid-like state at the timescales of somite formation [30], indicating that a different physical mechanism may be at play to shape somites. Here, we provide direct *in vivo* and *in situ* measurements of tissue mechanics during somite formation, spatiotemporal analysis of actomyosin dynamics, as well as computer simulations, to reveal the physical mechanism of somite formation in zebrafish development.

Results

Nascent somite boundaries shorten and straighten as somites mature. Since the defining morphological event initiating the formation of a new somite in the PSM is the appearance of its posterior boundary [9], we imaged its formation and monitored it over time by backtracking the forming somite boundary from its well-formed mature state (Fig. 1a,b; Methods; Supplementary Movie 2). The nascent posterior somite boundary appears initially contorted and sharpens over time. While the straight end-to-end distance of the nascent boundary, L_s, varies only slightly during somite formation (fixed largely by the mediolateral extent of the PSM), the boundary contour length L_c decreases by over 50% (Fig. 1b,c). This leads to the progressive straightening of the boundary (Fig. 1d), characterized by the ratio L_s/L_c, over approximately 1 hour and ends with a nearly perfectly straight somite boundary ($L_c/L_s \simeq 0.98$). In order to temporally align (and stage) somite formation in different embryos and perform statistical analysis, we took advantage of the fact that boundary straightening during the formation of a new somite (Fig. 1b,d) displays a sigmoid behavior (Fig. 1d), which has a well-defined timepoint (center point; t=0) characterizing the boundary straightening process (Methods). The observed progressive straightening of the prospective somite boundary suggests that mechanical stresses may be changing along the boundary during somite formation.

F-actin and myosin II accumulate at the forming somite boundary, albeit non-synchronously. Previous studies in *Drosophila* have shown that actin and myosin II accumulation at compartment boundaries are important for their formation and maintenance [19,31–34]. In zebrafish, enrichment of

F-actin at mature somite boundaries has been previously observed [35,36], suggesting that temporal changes in actomyosin activity may play a role in somite formation. To quantify their spatiotemporal dynamics at the forming boundary and relate them to the observed boundary straightening, we monitored actin and myosin II during boundary formation (Fig. 1e; Methods). Kymographs showing the spatiotemporal changes in F-actin and myosin II at the forming boundary indicate that both increase as the boundary shortens and straightens (Fig. 1f,g), with an average increase of approximately 180% and 150% in signal from S-2 to S2, respectively (Fig. 1h). While the increase in F-actin and boundary straightening occur simultaneously, accumulation of myosin II is delayed by approximately 15 min (Fig. 1d,h). Despite this delay, both F-actin and myosin II accumulate at the forming somite boundary as it straightens, suggesting that mechanical tension increases at the forming boundary during somite formation.

Mechanical stresses reorient in the tissue during somite formation. To directly quantify the temporal evolution of mechanical stresses in the tissue during somite formation, we employed magnetically-responsive oil droplets [30,37]. After injecting a fluorescently-labeled droplet in the PSM of zebrafish embryos at the 4-6 somites stage, we monitored it over time as somites formed (Fig. 2a,b; Methods; Supplementary Movies 3 and 4). To do so, we captured a 3D timelapse of each droplet, quantified its deformations using automated 3D reconstruction and analysis software [38,39] (Fig. 2c; Methods), and obtained both cell-scale and supracellular (tissue-scale) stresses after calibrating the droplet *in situ* and *in vivo* (Fig. 2c; Methods).

The average cell-scale stresses, namely those stresses occurring at cellular length scales [38]

(Methods), show no significant temporal change throughout somite formation, maintaining a value of approximately 200 Pa (Fig. 2d). These measurements are in agreement with previously measured values of cell-scale stresses in the PSM, which were shown to be spatially uniform in the tissue [30]. In contrast, tissue-scale stresses, obtained from the ellipsoidal mode of droplet deformation [38], displayed changes in both magnitude (Fig. 2e) and orientation (Fig. 2f,g) as the somites formed, revealing changes in mechanical stress anisotropy in the tissue. Before somite formation began ($t = -60$ min; B-3), droplets were initially oriented along the AP axis in the PSM due to the presence of mediolateral (ML) stress anisotropy, as previously reported [30]. As somite formation proceeded, tissue-scale anisotropic stresses substantially decreased (from 62 ± 15 Pa at B-3 to 35 ± 11 Pa at B-1) and reached a minimum just before B-1 ($t = 0$), with the direction of stress anisotropy changing in the process (Fig. 2e,g). After B-1, the magnitude of stress anisotropy strongly increased, reaching values (134 ± 48 Pa) 200% larger than those in the PSM, and the droplet aligned with the direction of the future somite boundary (Fig. 2g). These stress measurements show that tension along the nascent somite boundary progressively increases and competes with the ML stresses existing in the PSM (Fig. 2f), with the stress component oriented along the future somite boundary overcoming ML stresses at B-1 and increasing thereafter (Fig. 2h).

Mechanical stresses at the somite boundary strongly increase during somite formation. Since tissue-scale stresses reorient in the direction of the somite boundary and increase over time, stresses generated at the forming somite boundary may be responsible for driving somite formation. In order to measure the stress anisotropy at the somite boundary, we selected droplets located in the middle of the forming boundary (from the moment when a boundary is visible at B-1), and analyzed

the stress anisotropy between the direction defined by the somite boundary and the perpendicular one (Fig. 2i; Methods). The magnitude of boundary stress anisotropy is larger than tissue-scale stresses, indicating that maximal stresses in the tissue occur at the forming somite boundary (Fig. 2j). Moreover, boundary stresses increase over time, with their value doubling from just after B-1 (220 ± 33 Pa) to B3 (447 ± 49 Pa). The observed increase in boundary stress correlates with the progressive accumulation of actomyosin at the forming boundary (Fig. 2k), indicating that the measured spatial localization and temporal increase of boundary stresses are driven by the progressive actomyosin accumulation at the forming somite boundary.

Cell rearrangements show the regional fluidization of the tissue adjacent to the forming somite boundary. The measured values of boundary stress are larger than the previously measured residual (yield) stress in the PSM [30], suggesting that boundary stresses may fluidize adjacent tissue areas. Since plastic remodeling (or fluidization) of the tissue requires cell rearrangements (T1 transitions), we quantified the spatiotemporal dynamics of T1 transition rates during somite formation. To do so, we defined a quadrilateral grid on each somite (Fig. 3a,b; Methods), recorded the location and time of each neighbor exchange event (T1 transition; Fig. 3c), and analyzed the spatial distribution of neighbor exchanges within four 30 min periods from t=-60 min to t=60 min (B-3 to B1; Fig. 3d; Methods). The interior of the somite (excluding the regions directly adjacent to somite-somite boundaries; Fig. 3b,d) displayed uniform T1 transitions throughout somitogenesis, with a constant average rate equal to its value in the PSM before somite formation (from S-2 to S-1) (Fig. 3e; Methods). In contrast, T1 transition rates at the boundaries displayed significant changes during somite formation. The rate of T1 transitions in the tissue adjacent to the forming

posterior somite boundary showed a sharp ($>$ 2-fold) increase between t=0 (B-1) and t=30 min (B0), exactly the period when stresses along the somite boundary become dominant and boundary straightening occurs (Fig. 3f). This localized increase in T1 transitions reveals a regional fluidization of the tissue adjacent to the forming posterior somite boundary, caused by the large boundary stresses driving its shortening and straightening. Unlike this posterior region, the tissue adjacent to the anterior somite boundary displayed a significant drop in T1 transition rate after t=0 (Fig. 3g), decreasing by more than 3-fold from the average value in the somite interior and the PSM and indicating that the anterior tissue of the forming somite is rigidifying further than the PSM. These observations reveal spatiotemporal changes in the somite physical state over the course of somitogenesis, with the fluidization of the tissue adjacent to the posterior boundary occurring as the tissue surrounding the anterior boundary rigidifies. Together with previous measurements of stress relaxation in the paraxial mesoderm [30,40], our results indicate that at the timescales of somite formation (30 minutes) both the interior of the somite and its anterior boundary are in a solid state (albeit with a more rigid anterior boundary), while the posterior boundary is transiently fluidized during the physical segmentation of the PSM.

Active tension fluctuations at cell-cell contacts and an increase in somite boundary tension are necessary to reproduce somite morphogenesis. Our observations of increasing myosin II and actin levels at the nascent somite boundary, concomitant with boundary straightening and increasing boundary stresses, strongly suggest that an increase in tension at the somite boundary mechanically drives segmentation events. To test this hypothesis, we performed simulations of the mechanics of somitogenesis using an active foam description [40] (Methods). Starting from a popu-

lation of cells in a rectangular geometry (Fig. 4a), we defined different cell-cell contacts depending on whether they are located at the lateral boundary, at a somite boundary (heterotypic contacts) or in neither of those (homotypic contacts). To computationally account for our observations that cell-scale stresses do not change in time and that boundary stresses increase, we set the average value of homotypic tensions to a constant T_0, and made the average tensions at heterotypic cell-cell contacts, T_H, undergo sequential ramp ups (from T_0 at B-3 to a maximal value T_M at B1) following the observed increase in actomyosin at the somite boundary (Fig. 4b,c; Methods), including the observed delay in myosin II increase (Fig. 1h). Beyond their average value, cell-cell contact tensions fluctuate and drive cell-cell contact length fluctuations (Fig. 4d), as previously reported [30]. Consequently, we simulated tension fluctuations of constant amplitude ΔT and characteristic persistence time of 90 s, as observed experimentally [30]. Finally, we set the value of the tension at the lateral boundary to a constant T_L because measurements of F-actin and myosin II at the lateral boundary show no changes over time (Fig. 4e).

Values of the maximal heterotypic tension, T_M, larger than twice the value of the lateral boundary tension, T_L, namely $T_M > 2T_L$, led to complete somite separation (Fig. 4f). Below this threshold ($T_M < 2T_L$), adjacent somites shared a boundary of finite length (Fig. 4f; Supplementary Movie 5), with its straightness depending on how much heterotypic tensions increase at the somite boundary (T_M/T_0), irrespective of the value of the tension T_L at the lateral boundary (Fig. 4g,h). Increasing heterotypic tension up to 3 times homotypic tensions ($T_M/T_0 = 3$) efficiently straightened the somite boundary, but not much more above this value (Fig. 4h).

Beyond the increase of tension at the forming somite boundary, boundary straightness depended also on the magnitude of active tension fluctuations, $\Delta T/T_0$. The somite boundary could not straighten to experimentally observed values without tension fluctuations (Fig. 4i), as in this case the only cell rearrangements present were those induced by the tension increase at the somite boundary, with no cell rearrangements facilitated by active tension fluctuations [40]. Increasing the magnitude of tension fluctuations up to approximately $\Delta T/T_0 \simeq 0.6$ led to more straight somite boundaries (Fig. 4j). Beyond this point, increasing tension fluctuations did not help straighten the somite boundary significantly more. Moreover, the statistical variation in boundary straightness was maximal for vanishing tension fluctuations (Fig. 4j), indicating large deviations from the straight boundary, and decreased with increasing fluctuations up to about $\Delta T/T_0 = 0.6$, defining a sharper somite boundary with minimal variation for this value. In contrast, deformities in somite shape (somite angle; Fig. 4k) and deviations from the midline (positional deviations; Fig. 4k) showed a minimum at $\Delta T/T_0 \simeq 0.7$. These results indicate the existence of an optimal value of tension fluctuations ($\Delta T/T_0 \simeq 0.6 - 0.7$) leading to maximally robust somite formation.

Fitting the experimentally observed temporal increase in boundary straightness and its maximal observed value, we found best agreement between simulations and observations for $T_M/T_0 \simeq 3$ and $\Delta T/T_0 \simeq 0.6$. To estimate the value of the cell tension at the lateral boundary, T_L, we measured the angles θ_H and θ_L formed by two cells forming heterotypic and homotypic contact, respectively, at the lateral boundary (Fig. 4l). While the angle θ_L remains constant and close to 180 (flat lateral boundary) away from the somite boundary, the angle θ_H at the forming somite boundary decreases significantly throughout somitogenesis (Fig. 4m), in line with our measurements of

actomyosin accumulation at the forming boundary and increase in boundary stress. The value of θ_H at B1 allowed us to determine the value of T_L/T_0, locating wild type zebrafish somitogenesis in the parameter space (Fig. 4f). These results indicate that cells at the somite boundary increase the boundary tension during somite formation to the minimal value necessary to fully straighten the boundary, and that cells in the tissue generate an optimal level of active tension fluctuations to ensure robust somite morphogenesis.

Discussion

Altogether, our experimental and computational results show that somites are physically set apart from the PSM by an actomyosin-driven increase in anisotropic stress at the forming somite boundary that fluidizes the immediately adjacent tissue, thereby enabling tissue remodeling and the shaping of the somite. Moreover, we find that zebrafish somitogenesis occurs with close to optimal cell-cell contact tension fluctuations, which help robustly define straight somite boundaries with minimal morphological somite defects.

In contrast to observations using tissue explants suggesting that somites may form from a mere increase in tissue tension all around the fluid-like somite tissue, our results indicate that somites are physically segmented from the solid-like PSM following a highly localized increase in actomyosin-generated tension at the forming somite-somite boundary (between B-1 and B0), with no change in actomyosin-generated tension at the lateral boundary. In addition, we find that the somite interior remains in a solid-like state (as the PSM) during somite formation, with fluidization

occurring only in the tissue immediately adjacent to the straightening posterior boundary. Rather than the rounding of fluid-like tissue, somites seem to physically form by a sharp increase in tension at the forming somite boundary that drives a transient and localized tissue fluidization to facilitate tissue remodeling as the somite is sculpted. While our simulations of the physical process of somite formation reproduce both elongated somites that maintain contact, as observed in zebrafish, as well as round separated somites, resembling those recently observed in trunk organoids [41], it remains to be seen if this physical mechanism of somitogenesis is shared across vertebrate species. It is possible that similar physical events occur in distinct species, albeit with different cell behaviors and molecular control, as suggested by the observed differences in somite actin distribution in amniotes [17].

The observed actomyosin accumulation at the somite boundary is reminiscent of boundary formation in other systems [19,31–33], where actomyosin accumulation at the boundary has been shown to maintain separate physical compartments of the tissue. However, in vertebrates, mature somite boundaries are characterized by the presence of extracellular matrix [20,23,42,43], indicating that the increase in boundary stresses reported here may be necessary to physically segment somites, but not for boundary maintenance. Understanding the role of actomyosin-driven boundary stress in the maintenance of somite boundaries will require further investigation.

The notion that mechanics can help achieve robust somitogenesis was recently put forward in the context of lateral symmetry between somites [28]. Albeit in a different context, our results support the idea that mechanics enables robust somite formation, as the amplitude of tension fluctuations

appears to be optimally tuned to enable maximal somite boundary straightening with minimal variation in boundary straightness and minimal somite morphological defects. This result indicates that tension fluctuations may play an important role in embryonic development, not only in the control of fluid-to-solid transitions [30,40], but also facilitating the robust sculpting of embryonic structures.

Our findings highlight the need to connect genetic and molecular aspects of somitogenesis with cell and tissue mechanics to obtain a holistic view of somite formation and, more generally, of how functional embryonic structures are sculpted during embryonic development.

References

1. Gilbert, S. F. *Developmental Biology, 10th Edition* (Sinauer Associates, Inc., 2014).

2. Tabata, T. & Takei, Y. Morphogens, their identification and regulation. *Development (Cambridge, England)* **131**, 703–712 (2004).

3. Stooke-Vaughan, G. A. & Campas, O. Physical control of tissue morphogenesis across scales. *Current opinion in genetics & development* **51**, 111–119 (2018).

4. Heisenberg, C.-P. & Bellaiche, Y. Forces in Tissue Morphogenesis and Patterning. *Cell* **153**, 948–962 (2013).

5. Guillot, C. & Lecuit, T. Mechanics of Epithelial Tissue Homeostasis and Morphogenesis. *Science (New York, NY)* **340**, 1185–1189 (2013).

6. Hubaud, A. & Pourquié, O. Signalling dynamics in vertebrate segmentation. *Nature reviews Molecular cell biology* 1–13 (2014).

7. Bénazéraf, B. & Pourquié, O. Formation and Segmentation of the Vertebrate Body Axis. *Annual review of cell and developmental biology* **29**, 1–26 (2013).

8. Dequéant, M.-L. & Pourquié, O. Segmental patterning of the vertebrate embryonic axis. *Nature reviews Genetics* **9**, 370–382 (2008).

9. Pourquié, O. Vertebrate Somitogenesis. In *Annual Review of Cell and Developmental Biology*, vol. 17, 311–350 (2001).

10. Pourquié, O. The segmentation clock: Converting embryonic time into spatial pattern. *Science* **301**, 328–330 (2003).

11. Jiang, Y. J. *et al.* Notch signalling and the synchronization of the somite segmentation clock. *Nature* **408**, 475–479 (2000).

12. Venzin, O. F. & Oates, A. C. What are you synching about? Emerging complexity of Notch signaling in the segmentation clock (2020).

13. Oates, A. C., Morelli, L. G. & Ares, S. Patterning embryos with oscillations: structure, function and dynamics of the vertebrate segmentation clock. *Development (Cambridge, England)* **139**, 625–639 (2012).

14. Mara, A. & Holley, S. A. Oscillators and the emergence of tissue organization during zebrafish somitogenesis. *Trends in cell biology* **17**, 593–599 (2007).

15. Cooke, J. & Zeeman, E. C. A clock and wavefront model for control of the number of repeated structures during animal morphogenesis. *Journal of Theoretical Biology* **58**, 455–476 (1976).

16. Durbin, L. *et al.* Eph signaling is required for segmentation and differentiation of the somites. *Genes & development* **12**, 3096–3109 (1998).

17. Nakaya, Y., Kuroda, S., Katagiri, Y. T., Kaibuchi, K. & Takahashi, Y. Mesenchymal-epithelial transition during somitic segmentation is regulated by differential roles of Cdc42 and Rac1. *Developmental Cell* **7**, 425–438 (2004).

18. Watanabe, T., Sato, Y., Saito, D., Tadokoro, R. & Takahashi, Y. EphrinB2 coordinates the formation of a morphological boundary and cell epithelialization during somite segmentation. *Proceedings of the National Academy of Sciences of the United States of America* **106**, 7467–7472 (2009).

19. Dahmann, C., Oates, A. C. & Brand, M. Boundary formation and maintenance in tissue development. *Nature Reviews Genetics* **12**, 43–55 (2011).

20. Jülich, D., Mould, A. P., Koper, E. & Holley, S. A. Control of extracellular matrix assembly along tissue boundaries via integrin and Eph/Ephrin signaling. *Development* **136**, 2913–2921 (2009).

21. Lackner, S., Schwendinger-Schreck, J., Jülich, D. & Holley, S. A. Segmental Assembly of Fibronectin Matrix Requires rap1b and integrin α5. *Developmental Dynamics* **242**, 122–131 (2013).

22. McMillen, P., Chatti, V., Jülich, D. & Holley, S. A. A sawtooth pattern of cadherin 2 stability mechanically regulates somite morphogenesis. *Current Biology* **26**, 542–549 (2016).

23. Naganathan, S. R. & Oates, A. C. Patterning and mechanics of somite boundaries in zebrafish embryos. *Seminars in Cell and Developmental Biology* 1–9 (2020).

24. Tlili, S. *et al.* Shaping the zebrafish myotome by intertissue friction and active stress. *Proceedings of the National Academy of Sciences of the United States of America* **116**, 25430–25439 (2019).

25. Bard, J. B. A traction-based mechanism for somitogenesis in the chick. *Roux's Archives of Developmental Biology* **197**, 513–517 (1988).

26. Packard, D. S. & Jacobson, A. G. Analysis of the physical forces that influence the shape of chick somites. *Journal of Experimental Zoology* **207**, 81–92 (1979).

27. Dias, A. S., De Almeida, I., Belmonte, J. M., Glazier, J. A. & Stern, C. D. Somites without a clock. *Science* **343**, 791–795 (2014).

28. Naganathan, S. R., Popovic, M. & Oates, A. C. Somite deformations buffer imprecise segment lengths to ensure left-right symmetry. *bioRxiv* 2020.08.14.251645 (2020).

29. Gallaire, F. & Brun, P.-T. Fluid dynamic instabilities: theory and application to pattern forming in complex media. *Philosophical transactions. Series A, Mathematical, physical, and engineering sciences* **375** (2017).

30. Mongera, A. *et al.* A fluid-to-solid jamming transition underlies vertebrate body axis elongation. *Nature* **561**, 401–405 (2018).

31. Umetsu, D. *et al.* Local Increases in Mechanical Tension Shape Compartment Boundaries by Biasing Cell Intercalations. *Current Biology* **24**, 1798–1805 (2014).

32. Landsberg, K. P. *et al.* Increased Cell Bond Tension Governs Cell Sorting at the Drosophila Anteroposterior Compartment Boundary. *Current Biology* **19**, 1950–1955 (2009).

33. Monier, B., Pélissier-Monier, A., Brand, A. H. & Sanson, B. An actomyosin-based barrier inhibits cell mixing at compartmental boundaries in Drosophila embryos. *Nature Cell Biology* **12**, 60–65 (2010).

34. Major, R. J. & Irvine, K. D. Localization and requirement for myosin II at the dorsal-ventral compartment boundary of the Drosophila wing. *Developmental Dynamics* **235**, 3051–3058 (2006).

35. Koshida, S. *et al.* Integrinα5-dependent fibronectin accumulation for maintenance of somite boundaries in zebrafish embryos. *Developmental Cell* **8**, 587–598 (2005).

36. Barrios, A. *et al.* Eph/Ephrin signaling regulates the mesenchymal-to-epithelial transition of the paraxial mesoderm during somite morphogenesis. *Current Biology* **13**, 1571–1582 (2003).

37. Serwane, F. *et al.* In vivo quantification of spatially varying mechanical properties in developing tissues. *Nature Methods* **14**, 181–186 (2017).

38. Gross, B., Shelton, E., Gomez, C. & Campàs, O. Stress, an automated geometrical characterization of deformable particles for in vivo measurements of cell and tissue mechanical stresses. *bioRxiv* (2021).

39. Shelton, E., Serwane, F. & Campàs, O. Geometrical characterization of fluorescently labelled surfaces from noisy 3D microscopy data. *Journal of Microscopy* **269**, 259–268 (2018).

40. Kim, S., Pochitaloff, M., Georgina-Stooke-Vaughan & Campas, O. Embryonic Tissues as Active Foams. *bioRxiv* (2020).

41. Veenvliet, J. V. *et al.* Mouse embryonic stem cells self-organize into trunk-like structures with neural tube and somites. *Science (New York, NY)* **370** (2020).

42. McMillen, P., Chatti, V., Jülich, D. & Holley, S. A. A Sawtooth Pattern of Cadherin 2 Stability Mechanically Regulates Somite Morphogenesis. *Current Biology* **26**, 542–549 (2016).

43. Jülich, D. *et al.* Cross-Scale Integrin Regulation Organizes ECM and Tissue Topology. *Developmental cell* **34**, 33–44 (2015).

44. Nüsslein-Volhard, C. & Dahm, R. *Zebrafish: A Practical Approach* (Oxford University Press, 2002).

45. Swinburne, I. A. *et al.* Lamellar projections in the endolymphatic sac act as a relief valve to regulate inner ear pressure. *eLife* **7**, 1–34 (2018).

46. Compagnon, J. *et al.* The notochord breaks bilateral symmetry by controlling cell shapes in the Zebrafish laterality organ. *Developmental Cell* **31**, 774–783 (2014).

47. Maître, J. L., Berthoumieux, H., Krens, S. F. G. & Salbreux, G. Adhesion functions in cell sorting by mechanically coupling the cortices of adhering cells. *Science* (2012).

48. Pourquié, O. & Tam, P. P. A nomenclature for prospective somites and phases of cyclic gene expression in the presomitic mesoderm. *Developmental cell* **1**, 619–620 (2001).

49. Schröter, C. *et al.* Dynamics of zebrafish somitogenesis. *Developmental Dynamics* **237**, 545–553 (2008).

50. Holtze, C. *et al.* Biocompatible surfactants for water-in-fluorocarbon emulsions. *Lab On A Chip* **8**, 1632–1639 (2008).

51. Lim, I. *et al.* Fluorous Soluble Cyanine Dyes for Visualizing Perfluorocarbons in Living Systems. *Journal of the American Chemical Society* **142**, 16072–16081 (2020).

52. Schindelin, J. *et al.* Fiji: an open-source platform for biological-image analysis. *Nature Methods* **9**, 676–682 (2012).

Acknowledgements

We thank all members of the Campàs group for their comments and help, and B. Shelby, G. Stooke-Vaughan, S.-T. Yen and the UCSB Animal Research Facility for help with zebrafish care. We also thank Sean Megason (Harvard University) for kindly providing the Tg(actb2:memCherry2)^{hm29} transgenic line, and C.-P. Heisenberg (IST, Austria) for kindly providing the Tg(*actb2*:myl12.1-eGFP) and Tg(*actb2*:mCherry-Hsa.UTRN) transgenic lines. The Tg(actb2:mem-neonGreen-neonGreen)^{hm40}

line was generously provided before publication by Toru Kawanishi and Ian Swinburne in Sean Megason's lab (Harvard University). This work was supported by the National Institute of General Medical Sciences (R01GM135380 to EMS and OC) and the Eunice Kennedy Shriver National Institute of Child Health and Human Development of the National Institutes of Health (R01HD095797 to OC). We acknowledge support from the Center for Scientific Computing from the CNSI, MRL: an NSF MRSEC (DMR-1720256) and NSF CNS-1725797. The project was partially supported by the Deutsche Forschungsgemeinschaft (DFG, German Research Foundation) under Germany's Excellence Strategy – EXC 2068 – 390729961– Cluster of Excellence Physics of Life of TU Dresden.

Author Contributions

E.R.S. and O.C. designed research; E.R.S performed all experiments; E.R.S, B.G., M.P., R.W. analyzed data; S.K. performed all simulations; I.L. and E.M.S. synthesized fluorinated cyanine dyes; E.R.S. and O.C. wrote the paper; O.C. supervised the project.

Competing Interests

The authors declare that they have no competing financial interests.

Figure Captions

Figure 1: **Evolution of boundary morphology and F-actin and myosin II distributions at the forming boundary.** **a**, Sketches showing a lateral view of a 12-somite stage zebrafish embryo and a dorsal view of posterior tissues showing somites at different maturation stages (from S-2 to S2). **b**, Confocal sections of a forming somite in Tg(*actb2*:mem-neonGreen-neonGreen)^{hm40}embryos at S-1, S0 and S1, with its boundaries highlighted with dashed lines (posterior nascent boundary, yellow; other boundaries, black). A sketch of the forming posterior boundary is shown with the contour and end-to-end lengths, L_c and L_s, respectively, defined. **c-d**, Temporal evolution of L_c (orange; **c**), L_s (green; **c**) and the boundary straightness L_s/L_c (**d**), with sigmoid fits shown as continuous lines; $n = 110$ (22 somites; 5 timepoints) from 11 embryos. **e**, Confocal sections of the segmenting anterior PSM showing both membrane and F-actin (top) and membrane and myosin II (bottom) signals. Boundary masks are shown in yellow, and s is the contour distance along the boundary. **f**, Kymographs showing the temporal increase in F-actin (top) and myosin II (bottom) along boundary. Examples of the temporal evolution of the average F-actin (top) and myosin II (bottom) signals at the boundary are shown together with the time evolution of the boundary straightness. $n = 120, 100$ (12, 10 somites; 10 timepoints) from 6, 5 embryos (top, bottom). **g**, Relation between boundary straightness and F-actin (top) or myosin II (bottom) during somite formation. **h**, Temporal evolution of F-actin (top) and myosin II (bottom) average densities at the forming boundary. $n = 60, 50$ (top, bottom) (12, 10 somites; 5 timepoints) from 6, 5 embryos, respectively (**g-h**). Solid line shows sigmoid fit to average. Inset shows the temporal shift τ for F-actin (-1.9 ± 0.5 min) and myosin II (15.8 ± 0.5 min). Error bands = SE.

Figure 2: **Mechanical stresses during somitogenesis.** **a**, Confocal section of a droplet (magenta) at the boundary between somites S3 and S4 (membrane label, cyan; somite boundary B3 shown in yellow). **b**, Confocal sections of the temporal evolution (S-1 to S3) of a droplet at the somite boundary (top) and corresponding droplet stress maps (bottom). **c**, Sketch of the decoupling of cell and tissue scale stresses (Methods). **d-e**, Time evolution of cell-scale (**d**) and tissue-scale (**e**) stresses. $n = 20$ (4 droplets; 5 timepoints). **f**, Sketch showing the evolution of stresses during somitogenesis: increasing somite boundary stresses progressively compete with ML stresses in the PSM. Definition of the angles between droplet ellipsoidal elongation and the AP (blue) and somite boundary (yellow) directions, θ_{AP} and θ_{SB} respectively. **g-h**, Time evolution of the direction of droplet elongation (**g**), quantified by θ_{AP} (blue) and θ_{SB} (yellow), and of the projected magnitude of stresses (**h**) along the AP and somite boundary directions. $n = 20$ (4 droplets; 5 timepoints). **i-i'**, Confocal section of a droplet (stress colormap as in **b**) at a somite boundary (membrane label) with arrows indicating relative stresses on drop (**i**), and definitions of boundary belt and anterior and posterior caps (**i'**). Orange line indicates somite boundary (bottom). **j**, Temporal evolution of boundary stress. $n = 15$ (3 droplet; 5 timepoints). **k-l**, Boundary stress ($n = 30$) as a function of average F-actin (**k**) and myosin II (**l**) at the somite boundary ($n = 120, 100$ measurements from 12, 10 somites for **k**, **l**, respectively). Error bands = SE.

Figure 3: **Spatiotemporal changes in T1 transition rates during somite formation. a-b**, Confocal section of a somite (membrane label) with its boundary approximated as a quadrilateral (gray; **a**), and with a grid overlay (light gray; **b**) defining the different regions within the somite (yellow = anterior boundary, magenta = somite interior, cyan = posterior boundary) and neighboring tissue. **c**, Example of a T1 transition event shown with annotated confocal sections (membrane label). **d**, Time evolution of the T1 transitions' spatial distribution. **e-g**, Time evolution of average T1 transition rates for interior (**e**), posterior (**f**), and anterior (**g**) regions. $n = 42$ (14 somites, 3 time intervals) from 7 embryos. P-values were calculated using a Mann-Whitney U-test. Error bands = SE.

Figure 4: **Simulations of somite formation. a**, Initial state of somite formation simulation with prospective somites uniquely colored. Heterotypic (blue) and homotypic (black) cell-cell contacts, as well as the lateral boundary (maroon), are indicated. **b**, Schematic diagram showing tensions at lateral boundaries (T_L), heterotypic contacts (T_H), and homotypic contacts (T_0). **c**, Imposed time evolution of the normalized heterotypic and lateral tensions, T_H/T_0 and T_L/T_0, respectively, with T_H saturating to a maximal value T_M. **d**, Normalized frequency of the magnitude of cell-cell contact length fluctuations in the anterior PSM (reanalyzed from [30]). Inset shows junction length changes in 1 min interval. **e**, Confocal sections showing the F-actin (top) and myosin II (bottom) density during somite formation (left) and the time evolution of their average density at the lateral boundary (right). Individual somite measurements in light circles, averages in dark squares; $n = 6, 6$ somites (actin, myosin; $-60 < t < -45$ min); $n = 12, 8$ somites (actin, myosin; $t > -45$ min); error band = SE. **f**, Somitogenesis phase diagram, showing how somite formation depends on T_L/T_0 and T_M/T_0 ($\Delta T/T_0 = 0.6$). For $T_M/T_L > 2$ somites completely separate (cyan circle; cyan rectangle showing configuration, right). For $T_M/T_L < 2$, somites do not completely separate and share a boundary with a maximal straightness (color coded value at B1) that depends mostly on T_M (for fixed $\Delta T/T_0$). Configurations for parameter values estimated from experiments ($T_L/T_0 = 1.75$, $T_M/T_0 = 3$, $\Delta T/T_0 = 0.6$; purple, middle) and limiting case with no boundary tension increase ($T_M/T_0 = 1$; orange, bottom) are shown. **g-i**, Experimental (black circles) and simulated (lines) time evolution of boundary straightness L_s/L_c. Simulations for different values of T_M/T_0 (**g**; same color code as in **f**; $\Delta T/T_0 = 0.6$). Maximal boundary straightness (**h**; boundary straightness at B1, $L_s/L_c\,(B1)$) as a function of T_M/T_0 for different T_L/T_0 values ($\Delta T/T_0 = 0.6$), showing no significant effects of the lateral tension on boundary straightening. Simulations for different magnitudes of tension fluctuation $\Delta T/T_0$ (**i**; $\Delta T/T_0 = 0$ (green) ,$\Delta T/T_0 = 0.6$ (purple), $\Delta T/T_0 = 1.2$ (blue); $T_M/T_0 = 3$ and $T_L/T_0 = 1.75$). **j**, Dependence of the maximal boundary straightness (blue; $L_s/L_c\,(B1)$) and the standard deviation of maximal boundary straightness (yellow; $\sigma_{L_s/L_c(B1)}$) on $\Delta T/T_0$ ($T_M/T_0 = 3$ and $T_L/T_0 = 1.75$). **k**, Variability of final somite angle (top left) and position (top right) as a function of $\Delta T/T_0$ (bottom left). Final configurations of simulated somite formation for vanishing fluctuations ($\Delta T/T_0 = 0$; green) and large fluctuations ($\Delta T/T_0 = 1.2$; blue). Error band = SD in **g-k**. **l**, Confocal section showing the angle formed between adjacent cells from the same somite at the lateral boundary (θ_L) and cell on different somites (θ_H; at the somite boundary). **m**, Measured values of θ_L and θ_H at S0 and S2. $n = 12$ somites (6 embryos); error bar = SE.

Figure 5: **Physical mechanism of somite formation.** Sketch detailing the main events involved in mechanically forming a somite. A progressive accumulation of F-actin and myosin II at the nascent posterior boundary of the forming somite (S0) causes an increase in boundary tension that fluidizes the tissue adjacent to the forming posterior boundary (B-1 to B0), enabling tissue remodeling. Once mature (B0), the tissue adjacent to the boundary rigidifies again. Optimal actomyosin-generated tension fluctuations facilitate the process, enabling robust somite boundary formation. Somites are physically sectioned off the PSM by the boundary tension increase and fluidization at the posterior boundary.

Methods

Zebrafish husbandry and transgenic lines. Zebrafish (*Danio rerio*) were maintained as previously described [44]. Animals were raised and experiments were performed following all ethical regulations and according to protocols approved by the Institutional Animal Care and Use Committee (IACUC) at the University of California, Santa Barbara. Transgenic lines Tg(*actb2*:mem-neonGreen-neonGreen)^{hm40} or Tg(*actb2*:memCherry2)^{hm29} [45] were used to visualize cell membranes, and Tg(*actb2*:mCherry-Hsa.UTRN) [46] and Tg(*actb2*:myl12.1-eGFP) [47] were used to visualize F-actin and myosin II, respectively.

Imaging. Embryos were mounted in 1% low melting point agarose (E3 media containing 0.01% Tricaine) at approximately the 10 somites stage and imaged at 25°C using a laser scanning confocal microscope (LSM 710 Carl Zeiss Inc.). Images were acquired at 15 second intervals for *in situ* droplet actuation experiments and at 1 to 3 minute intervals for time lapse imaging of somite formation, depending on the experiment. All imaging of embryos was done using a $40\times$ water immersion objective (LD C-Apochromate 1.1 W, Carl Zeiss). Imaging of F-actin and myosin II was done with spatial resolution ranging from 0.35-0.69 µm. Volumetric images of droplets was done at 0.35µm spatial resolution, and 4.0 µm z-steps.

After timelapse imaging, embryos were removed from agarose and imaged laterally to determine the position of the droplet along the AP axis. All stress measurements were performed between the 14 and 16 somites stages.

Quantification of somite boundary morphology. Forming somite boundaries were identified and annotated manually using sequences of confocal sections of Tg(*actb2*:mem-neonGreen-neonGreen)^{hm40} or Tg(*actb2*:memCherry2)^{hm29} embryos. First, we identified the location of the mature somite boundary in the final frame of the timelapse sequence. Next, we identified the boundary in the previous frame in the sequence, using the most recently analyzed frame as a reference. At each frame, boundary annotations were recorded as ordered sets of coordinates. The boundary contour length L_c was computed by summing the length of line segments connecting the coordinates along the contour. The straight end-to-end distance of the somite boundary, L_s, was computed as the distance between the first and last coordinates of the contour. Somite-somite boundaries were annotated at 1 minute or 3 minute increments depending on the experiment, whereas lateral boundaries were traced at 15 minute intervals. Adaxial cell boundaries were not included in boundary annotations.

Temporal registration of different embryos and staging of somite formation. Data sets collected from different embryos were temporally aligned with each other using the temporal evolution of the straightness measure, namely $m_s(t) \equiv L_s/L_c$. For each somite boundary in each experiment, the measured straightness was fit to the function $m_s(t) = A/(1 + e^{(t-B)\times C}) + D$, where A specifies the amplitude, B specifies time of half-time between initial and final states, C specifies the ramping rate, and D specifies the baseline offset. For each embryo, we associated the half-time B with the time of stage B-1 of somite boundary formation (Fig. 1b), as the straightening corresponds to the nascent posterior boundary of somite S0 [48]. Experiments in different embryos were then temporally aligned by registering their half-times and shifting them all to t=0. Therefore, t=0 corresponds to the stage B-1 of somite boundary formation. The stages S(N) of somite

formation (S0 referring to the currently forming somite, S1 referring to the most recently formed somite, and so on) and their posterior (caudal) and anterior boundaries, namely B(N-1) and B(N) respectively, were denoted following established nomenclature [48] (Fig. 1b). Boundaries at stages B(N-1) (N = -2, -1, 1, 2, ...) occured at times $t = NT$ relative to stage B-1 ($t = 0$ min), with $T = 30.0 \pm 2.7$ min being the period of somite formation in our experiments (wild type zebrafish embryos at $25°$C [49]).

Quantification of F-actin and myosin II fluorescence signal at somite-somite and lateral boundaries. Quantification of the F-actin signal at the somite boundary was obtained using an outcross of Tg(*actb2*:mCherry-Hsa.UTRN) and Tg(*actb2*:mem-neonGreen-neonGreen)^{hm40} to visualize F-actin and membranes simultaneously, whereas quantification of myosin II signal at the somite boundary was done using an outcross of Tg(*actb2*:myl12.1-eGFP) and Tg(*actb2*:memCherry2)^{hm29} to visualize myosin II and membranes simultaneously. Intensities of actin and myosin II along the boundary contour were computed from boundary coordinates (see above) and fluorescent images sequences using custom Matlab scripts. Traced boundary coordinates were converted into a Polyline ROI object, which was then converted into a binary array using the function createMask(). This binary array was then dilated with a disk shaped structuring element using the function imdilate(), resulting in boundary masks approximately 3 μm in width. These masks were used at each frame to compute the average signal intensity along the boundary at each timeframe. We determined if considerable photobleaching occurred in a given timelapse by quantifying the temporal evolution of the average signal intensity within control rectangular regions (of area $\simeq 3200\,\mu m^2$) in the PSM, where the average intensity is not supposed to change in time. If significant bleaching

was observed for a given sequence, a single exponential photobleaching curve was determined by nonlinear regression and a time dependent bleach correction factor was applied to measurements from that sequence. After photobleaching correction (if required), signal intensities at the somite boundary were normalized by the average intensity in the somite boundary before somite formation starts, namely within the [-60,-30] min time interval ($t = 0$ min, corresponding to B-1).

Kymograph visualization of F-actin and myosin II signals at the somite boundary. For each column corresponding to a time point in the sequence, the fluorescent actin (or myosin) signal was measured along the somite boundary by averaging intensities within a 3 μm diameter circular mask at an increment of 3 μm along the path specified by the annotated boundary. The kymograph shows the traced intensities along the boundary contour for each time frame (frame rate = 3 min).

Generation and injection of ferrofluid droplets. Ferrofluid droplets were prepared as previously described [30,37]. Briefly, DFF1 ferrofluid (Ferrotec) was diluted in filtered 3M Novec 7300 fluorocarbon oil. To prevent non-specific adhesion between cells and droplets, a fluorinated Krytox-PEG(600) surfactant (008-fluorosurfactant, RAN Biotechnologies [50]) was diluted in the ferrofluid at a 2.5% (w/w) concentration. A custom-made fluorous Cy5 dye was used to visualize the droplet (see below). The ferrofluid was calibrated before each experiment as previously described [37], so that the applied magnetic stresses are known. Once prepared and calibrated, the ferrofluid was injected into the lateral mesodermal progenitor zone between 4 and 6 somites stage to form droplets of approximately 30 µm in diameter, as previously described [30,37]. Imaging of droplets started at least 1.5 hours after the injection to let the tissue fully recover from it. Embryos were incubated

for 2 hours at 25°C following injection to allow for tissue recovery, as previously described [30].

Magnetic actuation of ferrofluid microdroplets. Actuation of ferrofluid droplets was performed as previously described [37]. Briefly, ferrofluid droplets were actuated by a uniform and constant magnetic field to deform the droplet and apply stresses in the surrounding tissue. The magnetic field was applied for 20 minutes and subsequently turned off. The droplet interfacial tension γ was measured in each experiment *in situ* and *in vivo* from these actuation experiments, as previously described [30,37].

Generation of fluorinated cyanine dye for droplet imaging. To visualize ferrofluid droplets and perform 3D stress measurements *in vivo* and *in situ*, we employed a custom-synthesized fluorous Cy5 dye. While fluorous Rhodamine dyes have been previously used to visualize droplets [30,37], longer wavelength dyes are preferred for full 3D reconstructions of droplets. The fluorous Cy5 was synthesized using a similar protocol as previously described [51]. Briefly, a branched fluorous ketone was reacted with phenyl hydrazine to produce a fluorous indole. A fluorous methylene indolene was generated by *N*-alkylation with a perfluoroalkyl iodide. The heterocycle was condensed onto malonaldehyde bis(phenylimine) monohydrochloride in the presence of a pyridine base in acetic anhydride to generate the fluorous Cy5. The dye was isolated by column chromatography in 9% yield. The synthesized fluorous Cy5 dye was then diluted in the ferrofluid at a final concentration of 25 μM. We have previously show that the dye is biocompatible and enables robust 3D measurements of mechanical stresses [51].

Measurements of cell-scale and tissue-scale stresses. Stresses were quantified from the deformations of droplets inserted in the tissues, as previously described [30,38]. Briefly, droplets were imaged in 3D using confocal microscopy and their shape was reconstructed in 3D using automated software [38,39]. Using the measured value of the interfacial tension for each droplet (see above) and the time evolution of the droplet geometry, we measured the time evolution of cell- and tissue-scale stresses, as detailed in reference [38]. Reported amplitudes of cell-scale stresses were obtained using the value $\alpha = 0.05$ in the analysis software [38] to remove the smallest and largest 5% values of stresses, as these extreme values are prone to noise.

Measurement of stresses at somite-somite boundaries. The magnitude of stress anisotropy generated at the somite boundary was quantified by comparing the stresses along the somite boundary to the stresses in the direction perpendicular to the somite boundary. To do so, we measured the stresses in different surface regions on the droplet. At each time point, we defined a belt region as the set of droplet surface coordinates located within 5 μm of the somite boundary plane, which was identified by hand at each timepoint. We also defined anterior and posterior caps as the two 10 μm diameter regions on the droplet most distant from the somite-somite plane.

Let H_{B}, H_{A}, and H_{P} refer to the sets of mean curvature measurements within the belted region, the anterior cap, and the posterior cap, respectively. The boundary stress, σ_{B}, reads

$$\sigma_{\mathrm{B}} = 2\gamma \left(H_{\mathrm{B}}^{\max} - \frac{\bar{H}_{\mathrm{A}} + \bar{H}_{\mathrm{P}}}{2} \right) , \tag{1}$$

where γ is the droplet interfacial tension, $H_{\mathrm{B}}^{\max}$ is the maximal mean curvature value within the boundary belt, and $\bar{H}_{\mathrm{A}}$ and $\bar{H}_{\mathrm{P}}$ are the average mean curvatures in the anterior and posterior caps,

respectively.

Quantification of T1 transition (neighbor exchange) rates. To measure the spatiotemporal distribution in T1 transitions during somite formation, embryos featuring a membrane label were imaged at 1 minute intervals for at least 2 hours, as described above. Temporal alignment relative to B-1 was determined as described above. Each sequence was first divided into 10 minute increments, and then a quadrilateral grid was defined on the somite at that interval, as shown in Fig. 3a,b. The grid divides a forming somite into 9 segments along the ML direction and 5 segments along the AP direction. Moreover, the grid is extended further two rows anteriorly and posteriorly. All observed T1 transitions were recorded within the grid for each sequence, from S-2 to S2 and classified in 10 minute increments. The grid was used to define three regions within a forming somite: anterior boundary, somite interior, and posterior boundary. The anterior boundary region is the anterior-most row located within the somite, the posterior boundary region is the posterior-most row located inside the somite, and the somite interior region corresponds to the inner three rows between the anterior and posterior regions. T1 rates were computed within each region for each sequence. In total 14 somite formation sequences from 7 unique embryos were used. Measurements from all sequences were used to compute averages and standard errors.

Measurement of angles at the lateral boundary. Measurements of angles between cells at the lateral boundary, both at the contact with the somite boundary and slightly anterior to it, were performed using FIJI [52], by obtaining the angle between two straight segments defined along the boundary.

Active foam simulation of somite formation. To model somite formation, we adapted the theoretical framework of active foam simulations [40]. For initial configurations, a rectangular slab of cells that consists of eight prospective somites is generated with open boundary conditions. Each somite contains approximately 40 cells, 8 rows of cells in the ML direction and 5 rows of cells in the AP direction. Initial somite boundary is specified by assigning a somite ID to individual cells. To match experimentally observed initial somite boundary straightness, cell ID at the somite boundary is randomly swapped until the boundary straightness matches with the experimental value at stage B-3. As this tissue region, the anterior PSM, is close to confluence, we simulated the system at confluence throughout somite formation.

The equations governing the dynamics of the system are the same as in reference [40] and were integrated using the Euler-Maruyama method. The ramp up of heterotypic tension is implemented as a temporal increase of the target (fixed point) tension for heterotypic cell-cell contacts. The heterotypic tension ramp up was applied sequentially to somite boundaries and delayed by 30 minutes between them to match the experimentally observed time of somite formation. Throughout the simulations, T1 transitions were applied if a junctional length became shorter than a critical length, as previously described [40].

Data availability. Source data supporting these findings are available upon request.

Code availability. The code developed for this manuscript is available upon request.

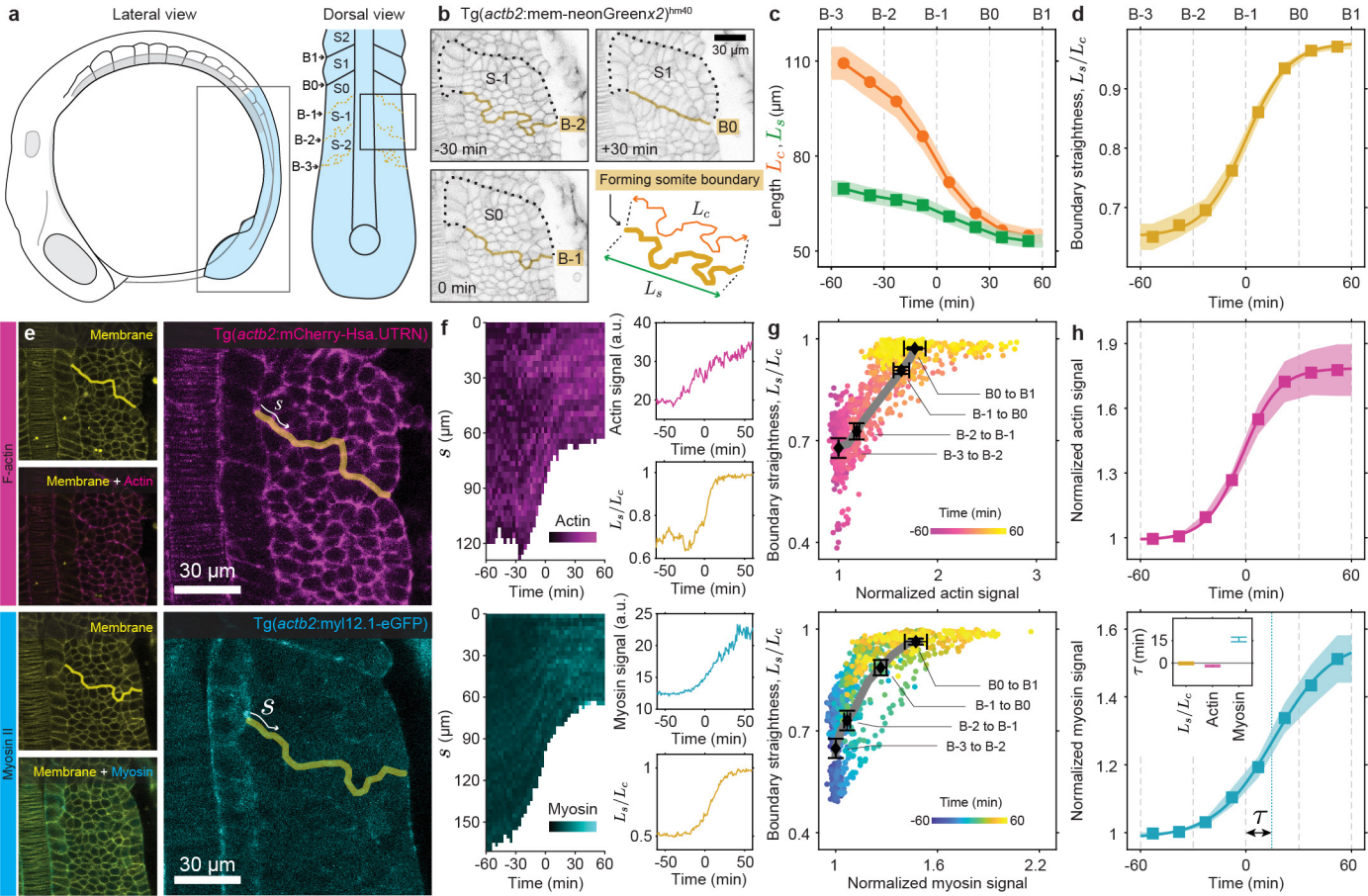
a
Lateral view
Dorsal view
S2
S1
S0
S-1
S-2
B1
B0
B-1
B-2
B-3
b
Tg(actb2:mem-neonGreenx2)hm40
S-1
B-2
-30 min
30 μm
S1
B0
+30 min
S0
B-1
0 min
Forming somite boundary
L_c
L_s
c
B-3
B-2
B-1
B0
B1
Length L_C, L_S (μm)
Time (min)
d
Boundary straightness, L_s/L_c
Time (min)
e
F-actin
Membrane
Membrane + Actin
Tg(actb2:mCherry-Hsa.UTRN)
s
30 μm
Myosin II
Membrane
Membrane + Myosin
Tg(actb2:myl12.1-eGFP)
s
30 μm
f
s (μm)
Actin
Actin signal (a.u.)
Time (min)
L_s/L_c
Myosin
Myosin signal (a.u.)
g
Boundary straightness, L_s/L_c
B0 to B1
B-1 to B0
B-2 to B-1
B-3 to B-2
Time (min)
Normalized actin signal
Normalized myosin signal
h
Normalized actin signal
Normalized myosin signal
τ (min)
H
L_s/L_c
Actin
Myosin
τ
Time (min)

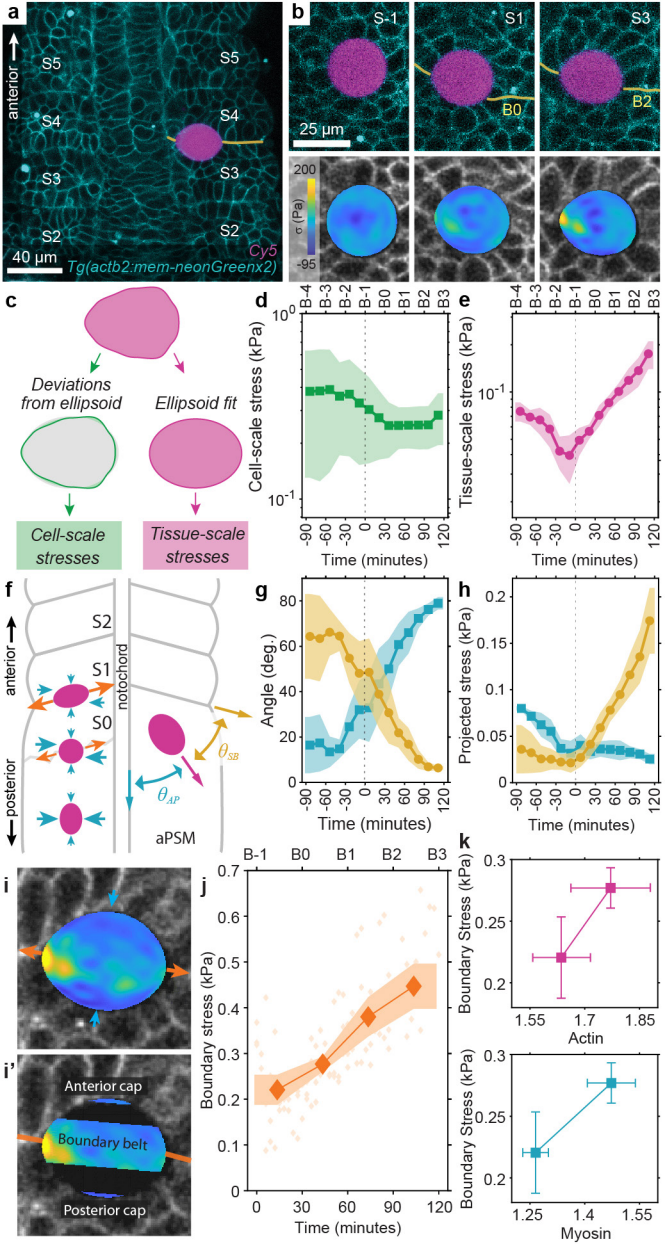
a
anterior
S5
S5
S4
S4
S3
S3
S2
S2
40 μm
Cy5
Tg(actb2:mem-neonGreenx2)
b
S-1
S1
S3
B0
B2
25 μm
200
σ (Pa)
-95
c
Deviations from ellipsoid
Ellipsoid fit
Cell-scale stresses
Tissue-scale stresses
d
Cell-scale stress (kPa)
Time (minutes)
e
Tissue-scale stress (kPa)
Time (minutes)
B-4
B-3
B-2
B-1
B0
B1
B2
B3
f
S2
S1
S0
anterior
posterior
notochord
aPSM
g
Angle (deg.)
Time (minutes)
h
Projected stress (kPa)
Time (minutes)
i
i'
Anterior cap
Boundary belt
Posterior cap
j
Boundary stress (kPa)
Time (minutes)
k
Boundary Stress (kPa)
Actin
Myosin

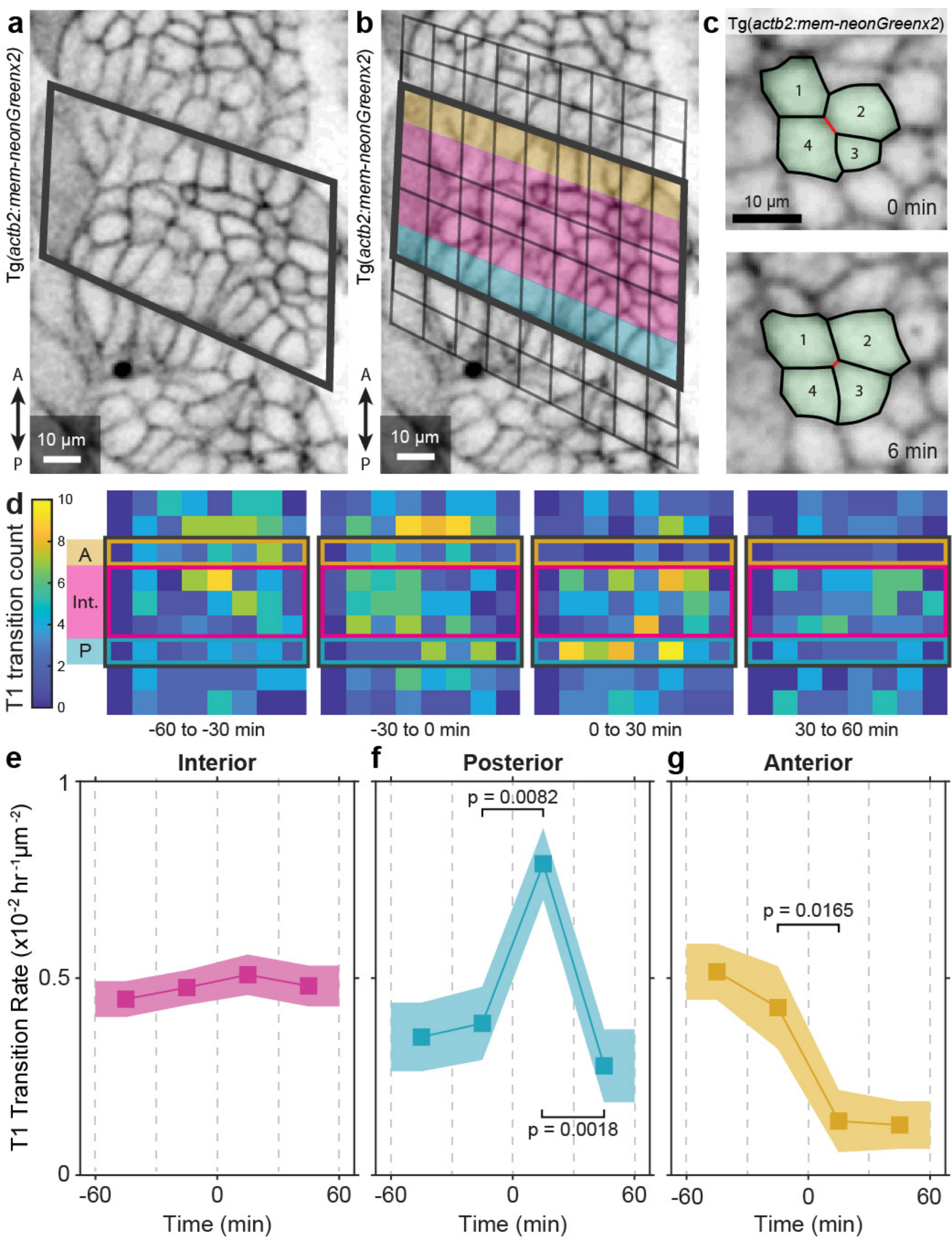
a
Tg(actb2:mem-neonGreenx2)
A
P
10 μm
b
Tg(actb2:mem-neonGreenx2)
A
P
10 μm
c
Tg(actb2:mem-neonGreenx2)
1
2
4
3
10 μm
0 min
1
2
4
3
6 min
d
T1 transition count
10
8
6
4
2
0
A
Int.
P
-60 to -30 min
-30 to 0 min
0 to 30 min
30 to 60 min
e
Interior
f
Posterior
p = 0.0082
p = 0.0018
g
Anterior
p = 0.0165
T1 Transition Rate (x10-2 hr-1μm-2)
1
0.5
0
-60
0
60
Time (min)
-60
0
60
Time (min)
-60
0
60
Time (min)

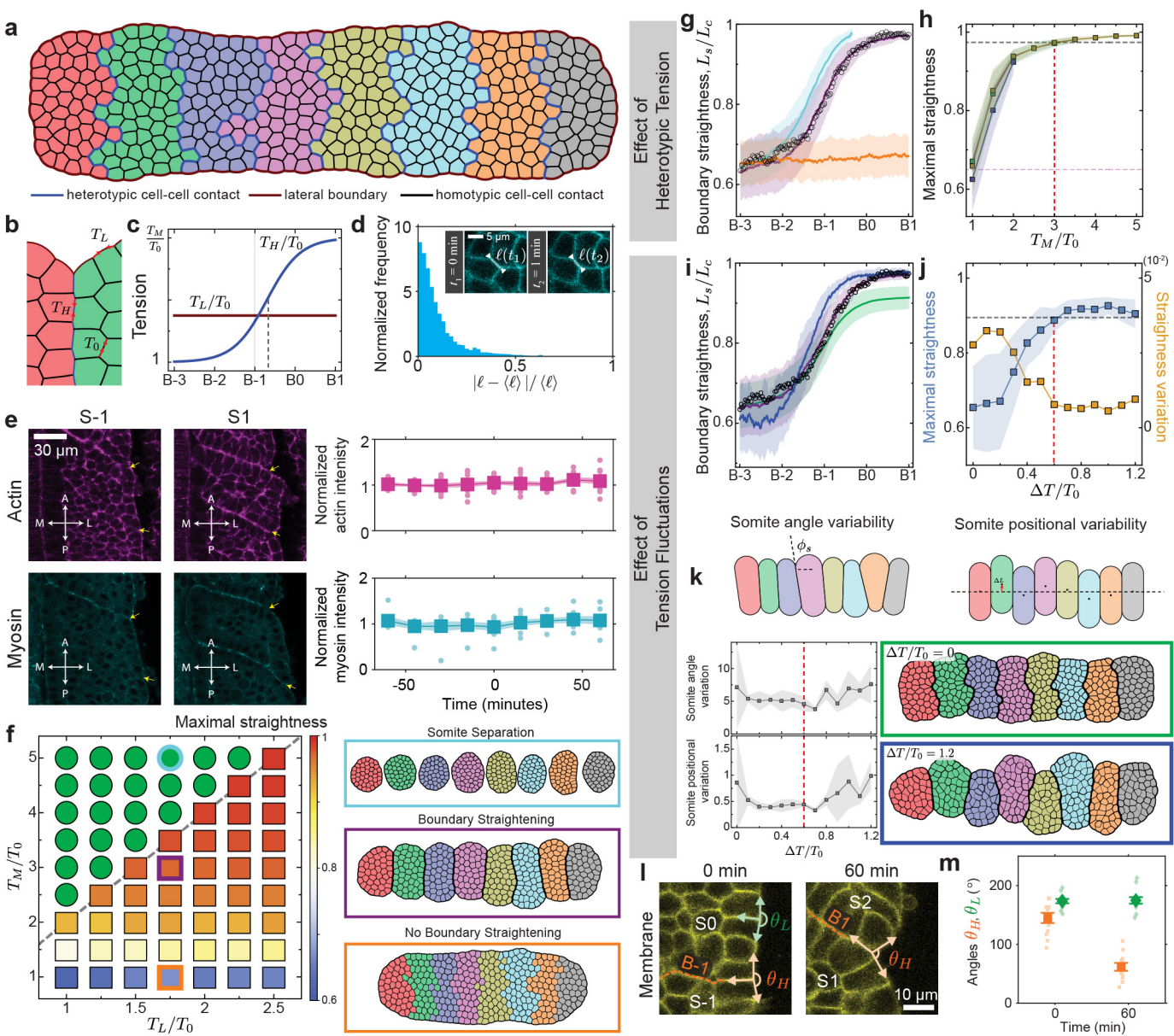
a
heterotypic cell-cell contact
lateral boundary
homotypic cell-cell contact
b
T_L
T_H
T_0
c
$\frac{T_M}{T_0}$
T_H/T_0
T_L/T_0
Tension
B-3 B-2 B-1 B0 B1
d
Normalized frequency
5 μm
t_1 = 0 min
t_2 = 1 min
$\ell(t_1)$
$\ell(t_2)$
$|\ell - \langle\ell\rangle| / \langle\ell\rangle$
e
S-1
S1
30 μm
Actin
Myosin
A
M
L
P
Normalized actin intensity
Normalized myosin intensity
Time (minutes)
f
Maximal straightness
T_M/T_0
T_L/T_0
Somite Separation
Boundary Straightening
No Boundary Straightening
Effect of Heterotypic Tension
g
Boundary straightness, L_s/L_c
h
Maximal straightness
T_M/T_0
Effect of Tension Fluctuations
i
Boundary straightness, L_s/L_c
j
Maximal straightness
Straightness variation
(10^{-2})
$\Delta T/T_0$
k
Somite angle variability
Somite positional variability
ϕ_s
ΔL
Somite angle variation
Somite positional variation
$\Delta T/T_0 = 0$
$\Delta T/T_0 = 1.2$
l
0 min
60 min
Membrane
S0
S-1
B-1
S1
S2
B1
θ_L
θ_H
10 μm
m
Angles θ_H, θ_L (°)
Time (min)

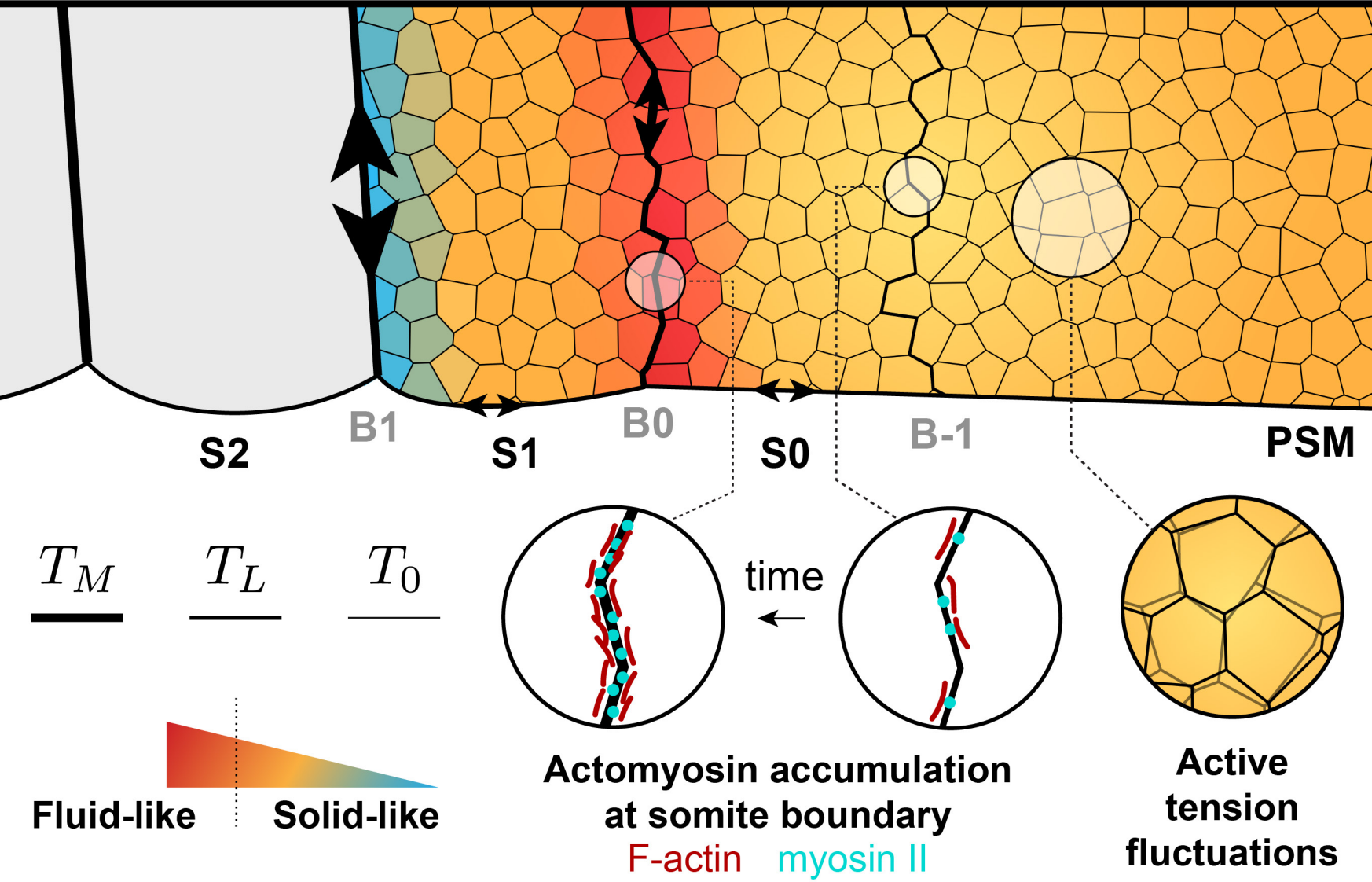
S2
B1
S1
B0
S0
B-1
PSM
T_M
T_L
T_0
Fluid-like
Solid-like
time
Actomyosin accumulation
at somite boundary
F-actin
myosin II
Active
tension
fluctuations